Supporting Information

for

Investigations of Heme Distortion, Low-Frequency Vibrational Excitations, and Electron Transfer in Cytochrome c

Yuhan Sun[1], Abdelkirm Benabbas[1], Weiqiao Zeng[1], Jesse G. Kleingardner[2], Kara L. Bren[2], and Paul M. Champion[1]*

[1]*Department of Physics and Center for Interdisciplinary Research on Complex Systems, Northeastern University, Boston, Massachusetts 02115*

[2]*Department of Chemistry, University of Rochester, Rochester, New York 14627-0216*

S1. Materials and Methods

Sample Preparation. Horse heart cytochrome c was purchased from Sigma-Aldrich and *Pseudomonas aeruginosa* (*Pa*) cyt c_{551} and its F7A mutant were prepared according to previously described methods.(1, 2) All samples were further oxidized with a small amount of potassium ferricyanide. Samples were freshly prepared in 0.05 M pH 7.0 potassium phosphate buffer before any spectroscopy measurements. The absorption spectra were recorded (U-4100, Hitachi) after the preparation procedure to ensure that all chemical modifications were achieved. For VCS experiments, the final concentration of ferric protein samples was adjusted to O.D. = 1 ± 0.05 in a 1 mm optical path length quartz sample cell at the selected excitation wavelength. The final concentrations of the samples are ~100 μM. The absorption spectra were also taken following the vibrational spectroscopy experiments to confirm the integrity of the samples during the laser exposure. For the kinetic measurements, the sample was passed through a PD-10 Sephadex G-25 column (GE Healthcare Bio-Sciences) twice to remove all remaining ferricyanide. Following this, the sample was sealed in a quartz cell and flushed with pure dry argon gas to remove oxygen. The sample used to measure the oxidation rate in the dark was prepared in 0.05 M potassium phosphate buffer by addition of sodium dithionite followed by centrifugation (Amicon Ultra-0.5 filter) to remove excess reductant and deoxygenation with argon gas. All experiments were performed at room temperature.

Resonance Raman. Resonance Raman spectra were obtained using a standard 90^0 light collecting geometry and a single grating monochromator (Acton SP2500i with 1800 g/mm UV holographic grating, Princeton Instruments). Details of the setup have been described elsewhere.(3) Samples were placed in a standard quartz cuvette (Precision

Cells, Inc.) and excited with ~ 5 mW of the 413.1 nm line from a krypton laser (Innova 300, Coherent).

Vibrational Coherence Spectroscopy. The femtosecond vibrational coherence spectroscopy system has been described in detail elsewhere (4, 5). Briefly, a 76 MHz laser pulse train at 412 nm was generated and split into two arms: pump and probe. The pump arm was modulated by an acoustic-optical modulator controlled by a lock-in amplifier at 1.5 MHz. A translation stage on the probe arm controlled the delay between the pump and probe pulses. The polarization of the pump and probe beams was adjusted to be perpendicular, allowing for both polarization and spatial filtering. The full width at half maximum of the pump and probe pulses was ~70 fs at the sample position. Both beams were focused into a spinning sample cell using a three inch lens in a near parallel geometry. After the sample, the beams were re-collimated and the pump light was spatially blocked and further extinguished by a polarization analyzer, so that only the probe beam, modulated by the pump, was detected. We used the open band scheme (5-8) to obtain the VCS spectra. A Si photodiode collected the entire spectral bandwidth of the probe pulse.

Data Analysis. The linear predictive singular value decomposition (LPSVD) data analysis method, which is used to extract the oscillatory components of the VCS signal, has been described in detail elsewhere.(9) To generate the power spectrum amplitudes from the time-domain oscillatory signal, we use a LPSVD algorithm that can fit both the monotonic background and the damped oscillations simultaneously, as described by $\sum_i a_i \exp(-t/\tau_i)\cos(\omega_i t + \phi_i)$. A few parameters can be controlled during the fitting procedure, such as the number of oscillations. The coherence coupling signal around time

zero was truncated before the fitting analysis. Data points within the truncated region (< 200 fs) were not included in the data analysis in order to eliminate the influence of the coherence coupling signal near time zero.

Photoreduction Kinetics Measurement. A crossed-beam transient absorption detection scheme was used to measure the photoreduction kinetics of *Pa* cyt c_{551} and horse heart (hh) cyt c. The laser beam (at 413.1nm, krypton laser, Innova 300, Coherent) was expanded by a Thor Labs ED1-C20-MD engineered diffuser that homogeneously illuminated the sample in a 1 mm pathlength quartz cell (cross-section 10 x 10 mm^2). The 10 mm radius of the diffused beam at the sample position was adjusted to overfill the sample to ensure homogeneous excitation of the entire sample. The power measured after expansion was 11 mW for *Pa* cyt c_{551} so that the photon flux was found to be J = 7.3 x 10^{15} photons/s-cm^2. For hh cyt c the power was increased to 68 mW and the flux was J = 4.5 x 10^{16} photons/s-cm^2. The absorption change of the sample due to photoreduction was recorded by a portable absorption spectrometer (Spectral Instruments, Inc. Tucson AZ), which was aligned about ~ 30° to the laser beam in order to avoid collecting scattering light. The experiment was repeated twice for each sample.

For each ferric *Pa* cyt c_{551} sample, two loaded quartz cells were prepared aerobically as described above for the oxidized species. One is kept in the dark compartment within the Hitachi spectrometer; the other was used for the photoreduction kinetic measurements. The "dark" sample contained no observable ferrous population over an experimental time longer than the photoreduction kinetic measurements. Other experiments using ferrous samples also shows no observable oxidized population on the same time scale. This indicates that the "dark" reduction and oxidation rates are much

smaller than the photon-induced electron transfer rates. All experiments were performed at least twice with fresh sample to assure the reproducibility of the results.

S2. Supplementary Data

Figure S2.1 Absorption spectra of ferric and ferrous *Pa* cyt c_{551} wild type.

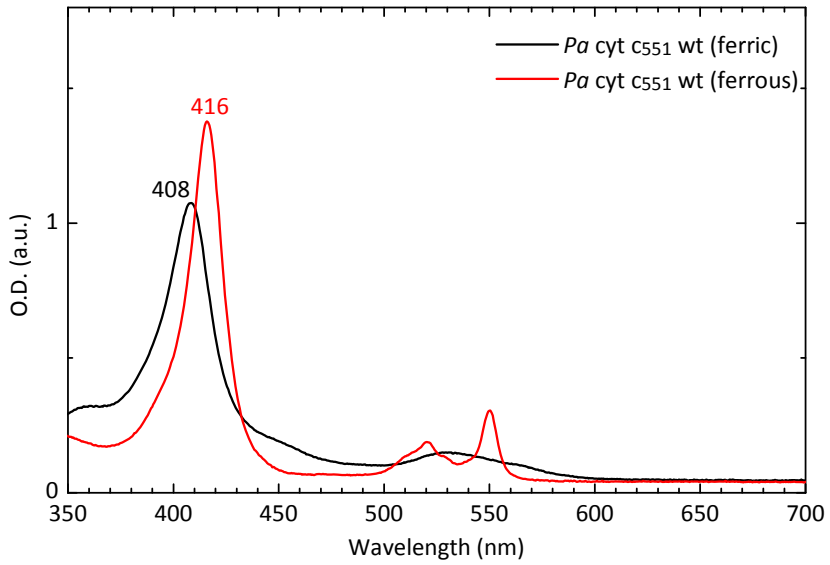

Figure S2.2 Absorption spectra of ferric and ferrous *Pa* cyt c_{551} F7A.

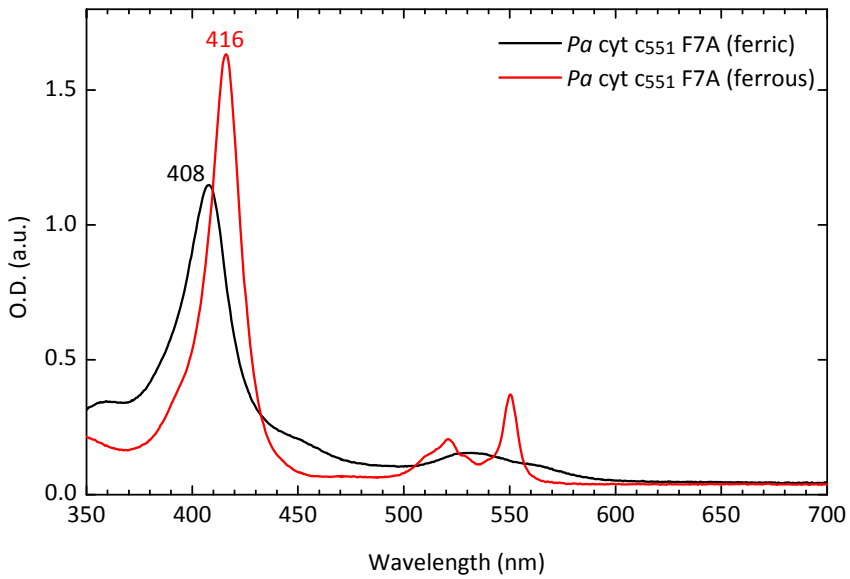

Figure S2.3 Resonance Raman spectra of oxidized *Pa* cyt c_{551} and its F7A mutant are compared with hh cyt c. Excitation wavelength is 413.1 nm. Power at the sample is 5 mW. The spectra are normalized with respect to the ν_4 peak. The observed spectra are aligned with the spectrum of hh cyt c. However, a few changes in the c_{551} Raman spectra are observed: reduced intensity of ν_9 (267 cm^{-1}), ν_{51} (shifted from 304 cm^{-1} to 310 cm^{-1}), ν_8 (decreased intensity at 350 cm^{-1}); ν_{50} shifts from 359 cm^{-1} to 366 cm^{-1}; the $\delta(C_\beta C_a C_b)$ peak shifts from 412 cm^{-1} to 419 cm^{-1}; and ν_7 shifts from 701 cm^{-1} to 706 cm^{-1}. The difference between the spectra of hh cyt c, c_{551} wt and the F7A mutant include a weaker γ_{21} mode when the heme is less ruffled. In other systems that do not have c-type hemes, such as NP4-CN(10, 11), NP-H_2O(3, 11), and LPO(12), this mode is not observed even though strong ruffling distortions are present.

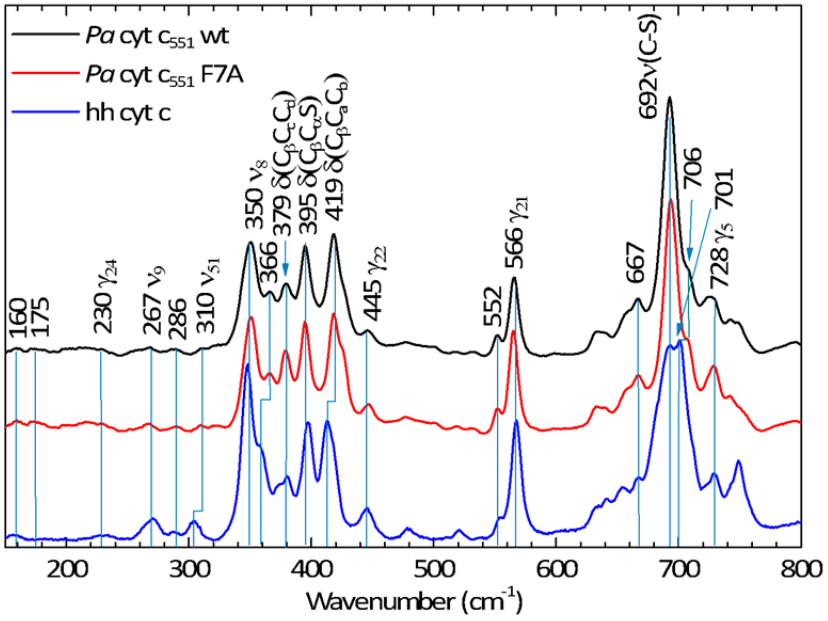

Figure S2.4 Resonance Raman spectra of ferric *Pa* cyt c_{551} wt and its F7A mutant. The excitation wavelength is at 413.1 nm and the power at the sample is 5mw. Spectra are normalized with respect to the ν_4 band at 1373 cm^{-1}. All mode positions agree very well between the two species, except γ_{15} (751 cm^{-1}), which seems to diminish in the F7A spectrum and ν_{11} (1560 cm^{-1}) which shifts to 1559 cm^{-1}. The mode γ_{21} (566 cm^{-1}) shifts to 565 and increases intensity in the F7A spectra.

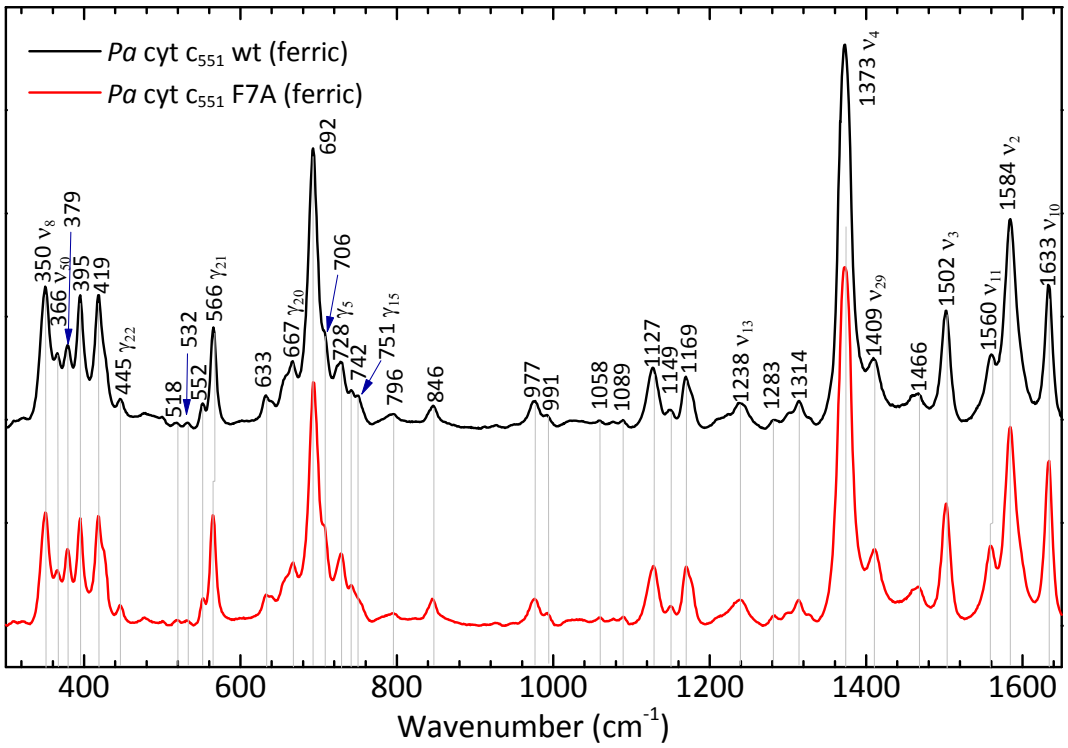

Figure S2.5 Resonance Raman spectra of ferrous *Pa* cyt c_{551} wt and its F7A mutant. The excitation wavelength is at 413.1 nm and the power at the sample is 5mw. Spectra are normalized with respect to the ν_4 band at 1361 cm^{-1}. All mode positions agree very well between the two species, except for modes at 396 cm^{-1} and γ_{11} (722 cm^{-1}), which shift to 394 cm^{-1} and 720 cm^{-1}, respectively.

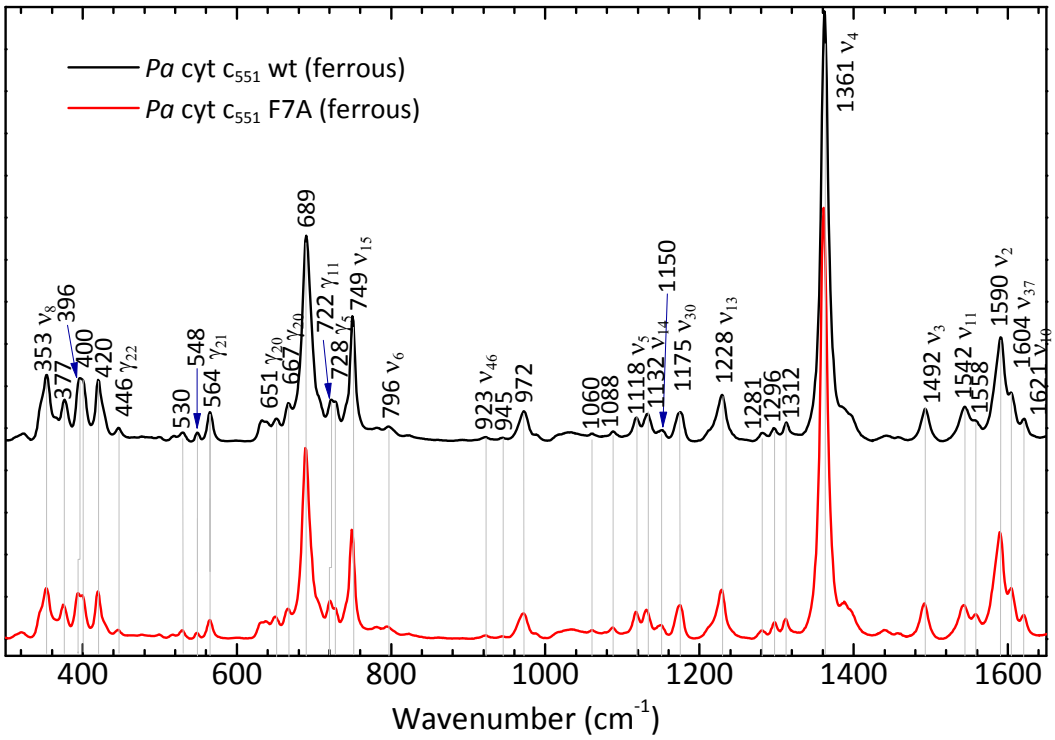

Figure S2.6 The intensity of γ_{21}, near 565 cm^{-1} in the resonance Raman spectra of ferric cyt c and *Pa* cyt c_{551} wt and F7A, is shown as a function of ruffling deformation. The relative intensity is obtained by normalizing each spectrum with respect to the intensity of its ν_4 band. The three data points are roughly linear as shown by the fit (solid line).

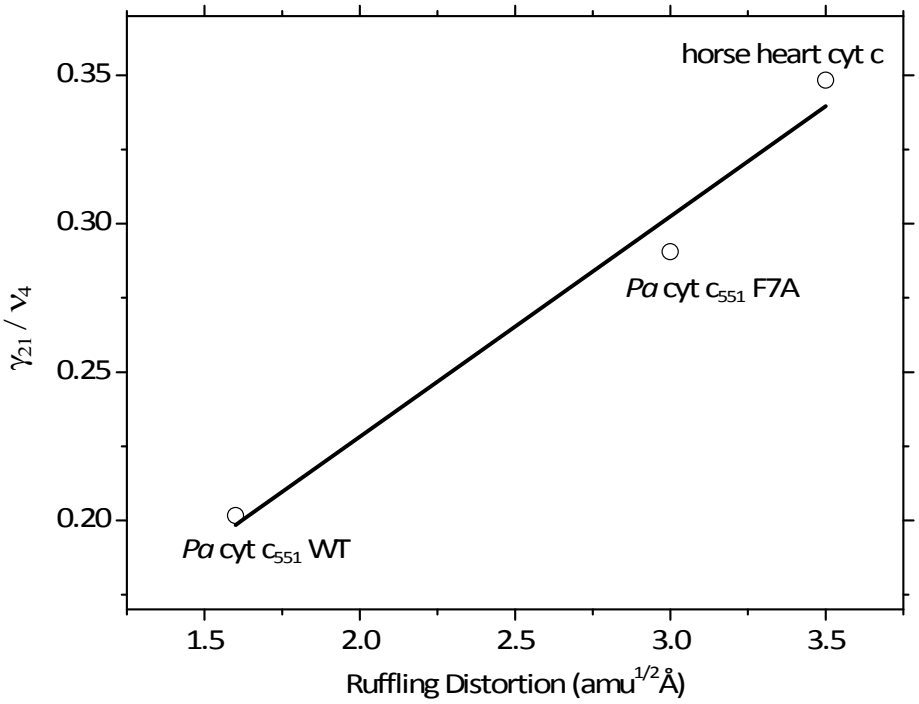

Figure S2.7 Soret resonance Raman spectra of intact bovine heart (A) and rat liver (B) mitochondria obtained with 413.1nm excitation in the low frequency region. The γ_{21} mode at 569 cm^{-1} disappears when the cytochrome is in the mitochondrial membrane(13) compared to the spectrum of ferrous cytochrome c in a buffer solution (C). (Reprinted by permission from *Biochemistry*. Copyright 2003 American Chemical Society).

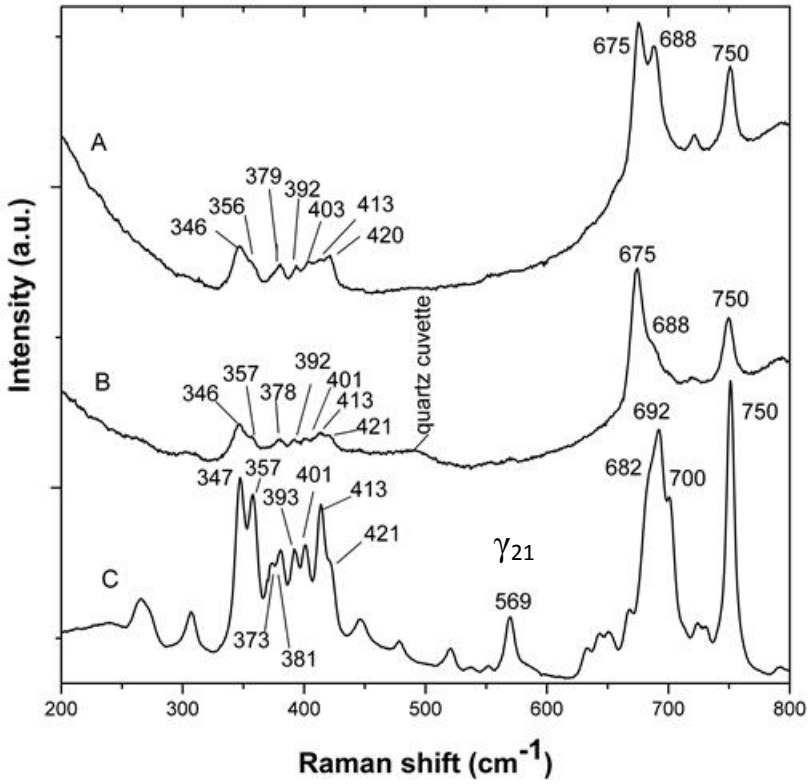

Figure S2.8 Comparison of resonance Raman spectra and the VCS results for ferric *Pa* cyt c_{551} wt (a) and its F7A mutant (b). The excitation wavelength for the Raman spectra is at 413.1 nm. The pump and probe wavelength used in the VCS experiment is 412 nm. The corresponding VCS oscillations are shown in the insert. The x-axis of the insert is time in picoseconds.

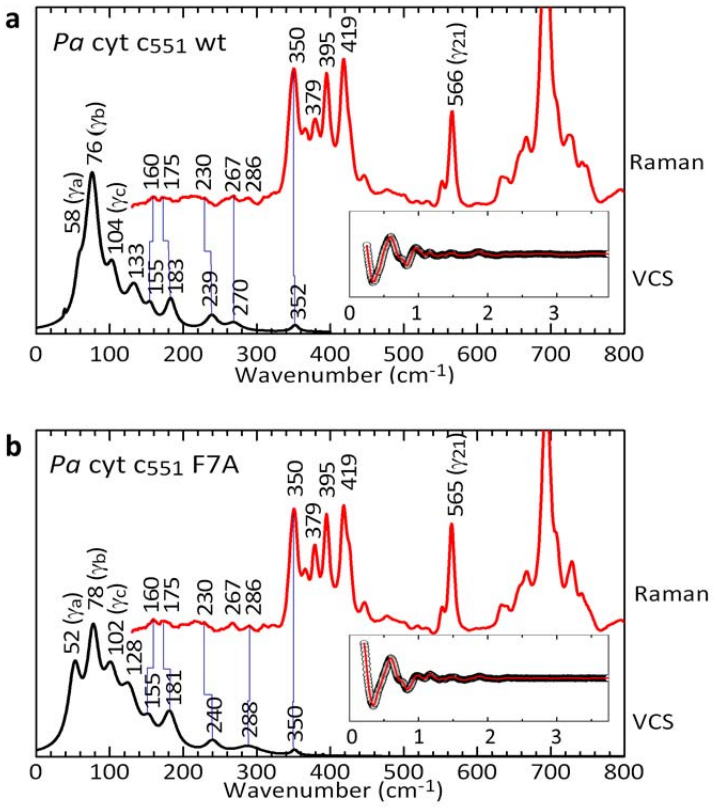

S3. Morse potential and frequency-distortion correlation.

Generally, under external forces from surrounding constraints, the potential can be described as:

$$U(q) = V(q) - qf_{ex} \tag{S3.1}$$

where f_{ex} is the force applied on the porphyrin along coordinate, q, and $V(q)$ is the ground state potential of the porphyrin in the absence of an external force. The equilibrium position, q_0, is determined by $dV(q_0)/dq_0 - f_{ex} = 0$. Thus, for small oscillations near q_0, the frequency is $\sqrt{U''(q_0)/\mu_r} = \sqrt{V''(q_0)/\mu_r}$, where μ_r is the reduced mass of the ruffling coordinate. For example, we can derive a correlation between frequency and distortion using a Morse potential. We let $V(q) = D_e(1 - e^{-aq})^2$ and, by setting the derivative of Eq. S3.1 to zero at the equilibrium position, q_0, we find $f_{ex} = 2aD_e(e^{-aq_0} - e^{-2aq_0})$. This leads to:

$$q_0 = -\frac{1}{a}\ln\left(\left(1 + \sqrt{1+s}\right)/2\right) \tag{S3.2}$$

where $s = -2f_{ex}/(aD_e)$ and exists on the domain [-1, 0] so long as f_{ex} and q_0 are taken to be positive. Thus the frequency of a small oscillation at q_0 is:

$$\omega = \sqrt{V''(q_0)/\mu_r} = \sqrt{2a^2D_e(2e^{-2aq_0} - e^{-aq_0})/\mu_r} \tag{S3.3}$$

As f_{eq} increases, the heme becomes more ruffled (q_0 increases) and the mode frequency ω decreases (from Eq. S3.2, aq_0 resides on the domain [0,-ln(0.5)]).

Using the heme ruffling mode frequency as a function of ruffling distortion shown in Fig. 3 of the text for cyt c, *Pa* cyt c_{551}, and NP4(3), the parameters in Eq. S3.3 are determined by fitting the data, resulting in $a = 0.09$ (amu$^{1/2}$ Å)$^{-1}$ and $a^2D_e/\mu_r = 3.15 \times 10^3\ (rad/s)^2$. The linear nature of Eq. S3.3 for small values of aq_0 can also be deduced by completing the square and expanding to find

$$\omega \approx \sqrt{\frac{2a^2 D_e}{\mu_r}}(1 - 3aq_0/2). \qquad \text{(S3.4)}$$

The following figure shows the Morse potential curves generated using the fitting parameters. The dashed line is the potential in the absence of an external force. Additional potential curves with different values of f_{ex} are also plotted in the figure. For the black solid curves from top to bottom, we have normalized D_e to unity and found the values for f_{ex} = 0.012, 0.020, 0.026, 0.032, 0.033, 0.036 (amu$^{1/2}$Å)$^{-1}$, which are determined by the ruffling distortion (q_0) of each data point in Fig. 3 of the main text.

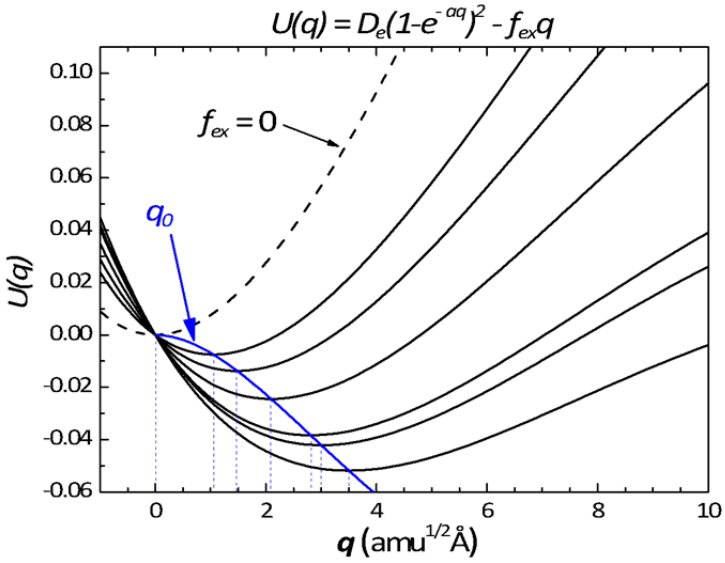

S4. Softening of the γ_a mode in cyt c unfolding.

It is necessary to note for hh cyt c, that the frequency of γ_a stays nearly unchanged in going from the folded to the unfolded state(9). This is surprising because of the anharmonic arguments discussed in S3 and the fact that, based on the reduced intensity of the ruffling mode and γ_{21}, the ruffling distortion is clearly smaller in the unfolded state(9). The reason for the lack of a frequency upshift upon unfolding is not precisely clear at this time, but it may be due to competing effects that arise from the

coupling between the heme ruffling mode and the axial ligand modes which are much less constrained in the unfolded state. Because the Met heme ligand in the native state is replaced by a His ligand in the unfolded state, and because the two His ligands are free to undergo torsional motions in the unfolded conformation(s), they become mixed with the ruffing mode (as revealed by DFT calculations). The increased reduced mass depresses the ruffling frequency and can counteract the frequency upshift that is expected from the simple anharmonic model presented above, which does not consider ligand exchange.

In the cyt c unfolding study(9), the reported frequency of γ_a stays nearly unchanged in going from the folded (γ_a = 44 cm^{-1}) to the unfolded state (γ_a = 45 cm^{-1}). Although absolute intensity measurements are only approximate, the decreased intensity of the ruffling mode upon unfolding suggested(9) that approximately one-third of the heme ruffling distortion remained in the unfolded form. This is presumably induced by the CXXCH motif(14), which remains intact upon unfolding. If the heme in the unfolded state has a ruffling deformation that is 33% of folded hh cyt c, it would correspond to ~ 1.2 $amu^{1/2}$Å, suggesting that the frequency of the ruffling mode should upshift to ~ 65 cm^{-1} in order to be consistent with Fig. 3 of the text. The lack of the expected upshift is probably due to the fact that there is ligand exchange in the unfolded state. The Met ligand in the folded state is replaced by another histidine so that a bis-His complex is formed with a very loosely packed structure. The absence of protein packing and hydrogen bonding means that the relative orientation of the distal histidines is not constrained in the unfolded state.

Using density functional theory (DFT) calculations, we investigated the ruffling mode frequency associated with the relaxed constraint on the His ligands in unfolded hh

cyt c. The frequency calculation was performed on a geometry optimized imidazole-porphine-imidazole structure, which mimics the bis-His coordination of heme in the fully unfolded hh cyt c at neutral pH. The optimized structure and the calculation details are given in Fig. S4.1. From the calculation, we find that the heme ruffling mode is strongly coupled to the rotation of the imidazole ligands about the N(imidazole)-Fe-N(imidazole) axis, which accounts for 31% of the total kinetic energy. Additional calculations on the same structure, but with the two axial imidazole ligands held fixed, showed that the ruffling frequency up-shifted from 60 cm^{-1} to 70 cm^{-1} in the constrained model. This result supports the suggestion that the relaxed constraints on the distal and proximal His ligands in the unfolded cyt c allows coupling between the His rotation about the N-Fe-N axis and the heme ruffling mode. This coupling increases the reduced mass of the ruffling mode and lowers its frequency in the unfolded state. Thus, the increased reduced mass of the ruffling mode in the unfolded bis-His state can counteract the upshift predicted by the simple anharmonic model discussed in Sec S3 and shown in Fig. 3 of the main text where no ligand switching or unfolding is involved.

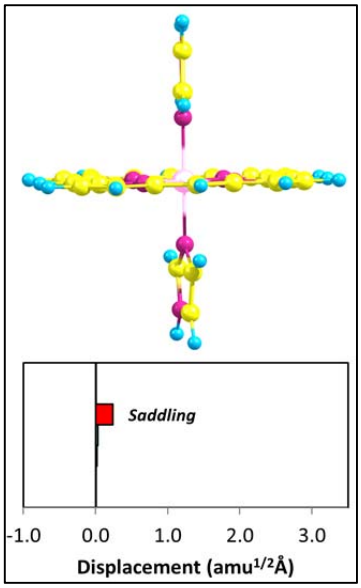

Figure S4.1 The DFT optimized Fe-porphine bis-histidine structure. Geometry optimization and harmonic frequency calculations were performed by using the DFT method at the B3-LYP level implemented in the Gaussian 09 software(15). Ahlrich's VTZ basis set(16) was employed for the iron, whereas the moderate 6-31G(d) basis set was used for H, C, and N atoms. Normal coordinate structural

decomposition (NSD) analysis was performed for both optimized structures and the major OOP distortions are shown. In the geometrically optimized structure, the two His ligands planes are nearly parallel to each other. The porphine is in a near planar structure with a small saddling distortion (0.2 $amu^{1/2}$Å). A displacement of 1 $amu^{1/2}$Å represents that the square root of the sum of squares of the displacements of Fe and 24 porphyrin (4N, 20C) atoms is 1 $amu^{1/2}$Å.

S5. Effect of donor amino acid positions.

In this section we consider the positions of aromatic amino acids that are likely electron donors for the photoreduction reactions in *Pa* cyt c_{551} and hh cyt c. The positions of the aromatic amino acids nearest the heme in *Pa* cyt c_{551} and its F7A mutant are seen in Fig S5.1. All aromatic groups for the *Pa* cyt c_{551} system are on the proximal side of the heme. As shown in the figure, the distances from Phe 34, Trp56 and Trp 77 to the heme are nearly unchanged by the F7A mutation. Tyr27 moves 0.3 Å perpendicular to the heme plane in F7A, but maintains basically the same distance (3.8-3.9 Å) to the closest heme meso carbon atom, due to the bending of the meso carbon as a result of the increased ruffling distortion in F7A. The distance from Tyr27 to the closest two beta pyrrole carbons is also nearly unchanged, suggesting that the overlap between the heme π and Tyr27 π orbitals is minimally affected.

The Phe7 residue that is mutated resides further from the heme and is about ~1.5x the distance from the heme as found for the aromatic residues in cyt c (see Table S5) where the photoreduction rate is an order of magnitude smaller. If Phe7 were the primary electron donor in *Pa* cyt c_{551}, we would expect to measure photoreduction cross-sections that are on the order of what we see in hh cyt c, or less. The fact that they are orders of

magnitude larger strongly indicates that F7 is *not* the primary electron donor. Moreover, the orientation of the Phe7 plane is perpendicular to the heme plane(17-19), which is consistent with the conclusion that it is not an efficient electron donor in *Pa* cyt c_{551}.

We have considered the possibility that either a single electron donor, or a set of multiple electron donors, is involved in the electron tunneling process. Fig. S5.2 shows the case for a single donor. A distance modulation, αq_0, associated with hole localization on the iron atom is also depicted. The maximum value of the modulation, $\alpha_{max} q_0$, can be found by assuming that other factors, such as the reorganization energy and driving force for the reaction are independent of the ruffling distortion (both λ and ΔG^0_{red} are expected to increase with ruffling, and therefore decrease the rate, which helps to set a maximum limit on the distance modulation). When this is done, it is possible to fit the photoreduction cross-sections as a function of q_0 with an exponential function involving the total tunnel distance, $k_{et} \sim \sigma_r \sim V_0 e^{-\beta r_0} e^{-\beta \alpha_{max} q_0} = C_0 e^{-\beta \alpha_{max} q_0}$. The reduction of the fit to include just q_0 is dependent on the fact that the distance r_0 is nearly identical in the wt and mutant *Pa* cyt c_{551} and very similar to what is found for the nearest neighbor aromatic donors in hh cyt c (see Table S5). Upon fitting the data in Fig. 4b of the text, we find $\beta \alpha_{max} = 2.4$ Å$^{-1} amu^{-1/2}$. Upon choosing a typical value of β =2 Å^{-1}, we find $\alpha_{max} = 1.2\ amu^{-1/2}$. With $q_0 = 1.58, 3.0, 3.5$ Å $amu^{1/2}$, we find that the maximum changes in tunnel distance modulation are ~ 1.9, 3.6, and 4.2 Å for *Pa* cyt c_{551}, its F7A mutant, and hh cyt c, respectively, which are on the order of the heme dimension. If β is reduced to 1.5 Å^{-1}, these distances increase to ~2.5, 4.8, and 5.6 Å^{-1}, respectively. If only the *Pa* cyt c_{551} rates are used in the analysis, in order to cancel the variations in protein structure due to hh cyt c as nearly as possible, we find α_{max} = [0.8-1.0] amu$^{-1/2}$, for β =

[2.0-1.5] $Å^{-1}$ and distance modulations of [1.2-1.6] Å and [2.3-3.0] Å, well within the heme radius. The value of α will drop below α_{max} when other ruffling dependent terms associated with the Marcus barrier are included. This maintains the distance modulation at, or below, the heme length scale and is consistent with the concept of hole localization on the heme and its ability to affect electron transfer rates.

In the case of multiple electron donors, their contributions must be summed so that, in terms of the maximum possible distance modulation, $\sigma_r \sim V_0\left(\sum_i e^{-\beta r_{0,i}}\right)e^{-\beta\alpha_{max}q_0}$. In the main text, we assumed that the term $\left(\sum_i e^{-\beta r_{0,i}}\right)$ was approximately the same for hh cyt c and *Pa* cyt c_{551} (i.e., the ratio of these terms in the different samples is much less than the observed 1-2 order of magnitude change in the rates). In order to justify this assumption, we have listed the values of $e^{-\beta r_0}$ for each aromatic amino acid in Table S5. From the listed values we find that the ratio between the values of $\left(\sum_i e^{-\beta r_{0,i}}\right)$ for hh cyt c and c_{551} is on the order of 2 and is essentially independent of whether single or multiple electron donors are considered. This is because the exponential drops off rapidly as the donor distance increases and the sum enters numerically, in a linear (non-exponential) fashion. The ratio between hh cyt c and *Pa* cyt c_{551} is 1.5 when only the closest amino acid is considered, 1.8 when all aromatic amino acids that are parallel to porphyrin plane are considered, and 1.9 when all aromatic amino acids are included. Since these values are smaller than the observed two order of magnitude change in photoreduction rate, it appears that the different arrangement and number of amino acids in cyt c compared to *Pa* cyt c_{551} does not play a significant role. The fact that the distance differences appear to favor *enhancement* of the hh cyt c rates by ~ a factor of 2, which is *opposite* to the observed rate change, justifies the assumption

used in the main text that the differing number and arrangement of the amino acids in hh cyt c is not the explanation for why its rate is so much slower than *Pa* cyt c_{551}.

In fact, we also recalculated the value of α_{max} using a correction factor to account for the small difference r_0 in hh cyt c. Using the heme edge to aromatic center distances and correcting for the different $r_0$value of the only closet aromatic amino acid in hh cyt c leads to $\alpha_{max} = 1.4\ amu^{-1/2}$ (using β=2.0 Å^{-1}). When all parallel amino acids are considered in the sum over donors in both *Pa* cyt c_{551} and hh cyt c, we find $\alpha_{max} = 1.5\ amu^{-1/2}$, and the same result is obtained if all aromatics are considered (both parallel and perpendicular). When the results using edge-to-edge distances are compared to the results using distances from the heme edge to the center of the amino acids (and we again correct for the small r_0 difference between hh cytc c and *Pa* cyt c_{551}), we recover $\alpha_{max} = 1.30 \pm 0.03\ amu^{-1/2}$ depending upon whether we include all aromatics, just the parallel, or just the nearest aromatic amino acid. Thus, we believe that the value $\alpha_{max} = 1.2 - 1.5\ amu^{-1/2}$ is robust, and independent of the donor model selected. If β is taken to be less than 2 Å^{-1}, this can increase the value of α_{max}, so we take α_{max}~$1.2 - 1.6\ amu^{-1/2}$ as discussed in the text.

Finally, we consider the possibility that the amino acid donor might change due to the heme ruffling. We note that the rate falls off rapidly for the aromatic amino acid donors, particularly in *Pa* cyt c_{551}, where there is a substantial increase in distance between the closest and second-closest amino acids (see Table S5). Correspondingly, there is a 10-fold difference in the overlap function. It is doubtful that changes in reorganization energy or free energy resulting from the change in ruffling would be enough to overcome this difference in distance, such that the farther amino acid becomes

the primary donor instead of the closer one. If the protein were able to "find" an optimal amino acid with appropriate reorganization energy and redox potential to optimize the rate as a function of ruffling, then hh cyt c should have the faster rates because of the closer and more available donors. Because there is no obvious reason to believe that the amino acids have significantly different lambdas and potentials in *Pa* vs. hh cyt c (they are the same functional groups, mostly buried in a hydrophobic protein), it seems unlikely that the extent of heme ruffling is somehow selecting more distant amino acid donors based on reaction free energies or lambdas (particularly in the case of hh cyt c). Thus, we suggest that it is simpler and more likely that heme ruffling alters the transport distance as depicted in Fig. S5.2.

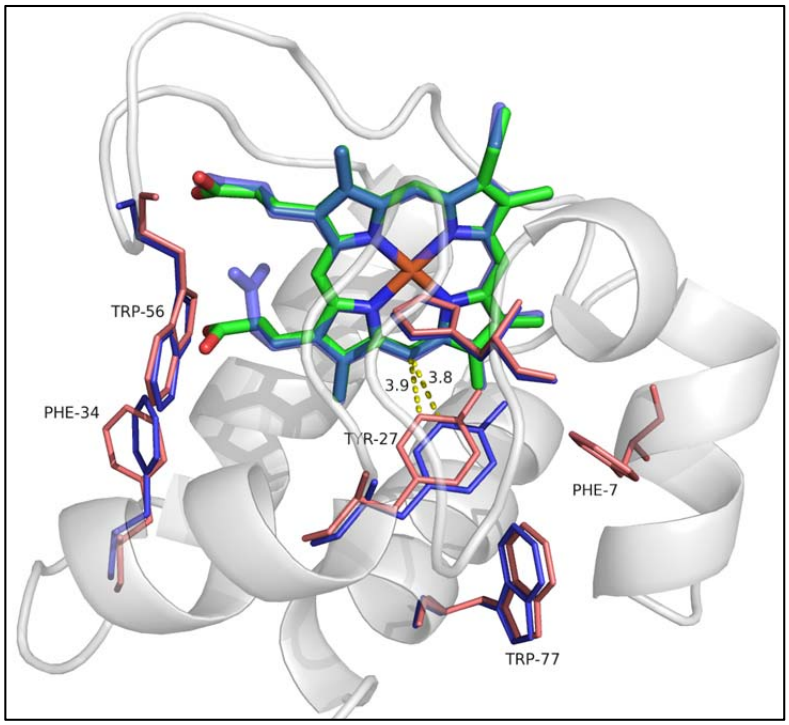

Figure S5.1 Overlap of *Pa* cyt c_{551} wt (PDB#351C) and the F7A mutant crystal structure(2) (PDB#2EXV). The aromatic residues are shown in stick format (wt in red color, F7A in blue color). The heme groups of wt and F7A nearly overlap with each other except for a rotation of one of the propionate groups. The carbon atoms of the wt heme group are shown in solid green format, while the heme group of the mutant is shown in a transparent blue color. For clarity, only the secondary structure of wt is shown.

Figure S5.2 Schematic diagram showing how the effective tunnel distance increases with the magnitude of the ruffing distortion (q_0) as the hole state localizes on the iron atom**.**

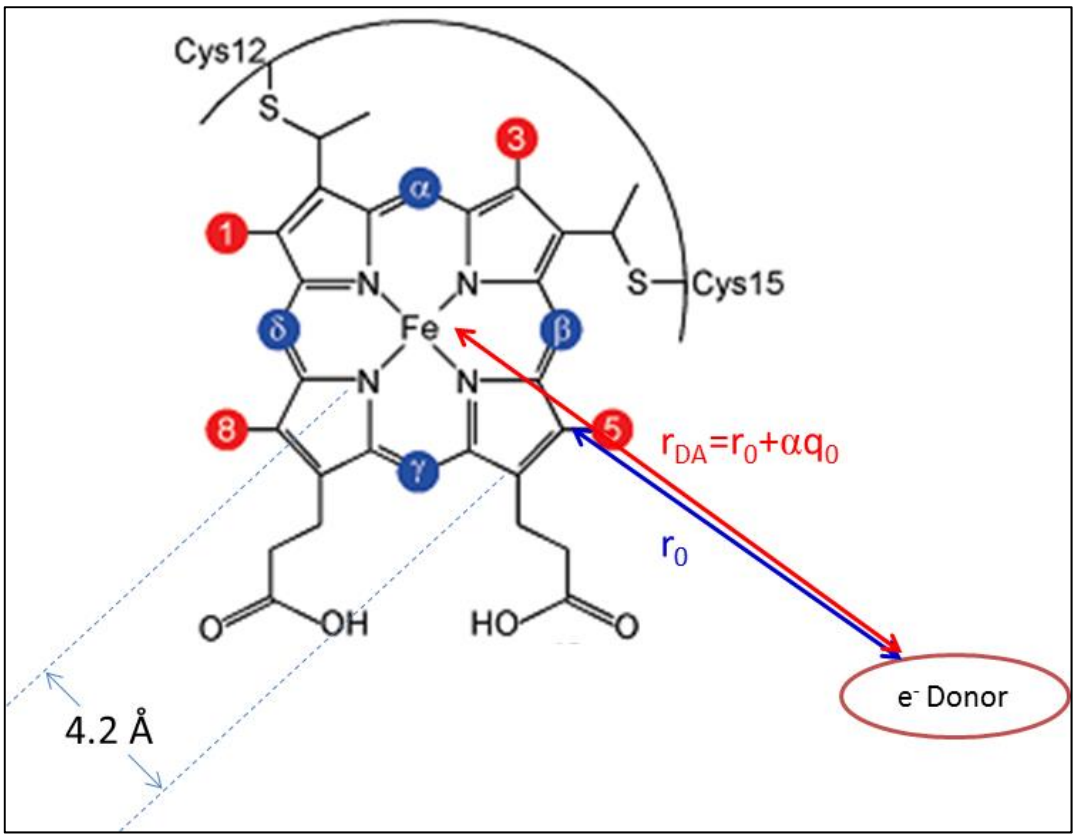

Table S5: Summary of aromatic amino acids in hh cyt c and *Pa* cyt c551 and their distance to Fe and to the closest C atom on porphyrin ring. The symbols // and ⊥ are used to crudely indicate the relative orientation of the aromatic amino acid rings with respect to the porphyrin ring.

Protein	Aromatic amino acids	Center Distance to Fe (Å)	Closest porphyrin carbon	Carbon distance† r_0 (Å)	Overlap function‡ $e^{-\beta r_0}$	Location and orientation to heme
hh cyt c	Phe82	7.3	Cα	4.1(4.6)	$2.8(1.0)\times10^{-4}$	Distal, //
	Tyr67	7.6	C_8	3.3(5.1)	$13.6(0.37)\times10^{-4}$	Distal, //
	Trp59	9.7	Pyrrole A	4.7(5.7)	$8.3(1.1)\times10^{-5}$	Distal, //
	Tyr74	13.1	C_7	9.2(10.5)	$10.2(0.76)\times10^{-9}$	Distal, ⊥
	Phe46	9	Pyrrole D	4.6(5.7)	$1.0(0.11)\times10^{-4}$	Proximal, //
	Phe10	9	C_1	5.1(6.3)	$3.7(0.34)\times10^{-5}$	Proximal, ⊥
	Tyr48	9.7	C_γ	5.2(6.5)	$3.0(0.23)\times10^{-5}$	Proximal, ⊥
	His26	11.6	C_6	9.6(10.0)	$4.6(2.1)\times10^{-9}$	Proximal, //
	Tyr97	13.9	C_1	9.1(10.4)	$12.5(0.93)\times10^{-9}$	Proximal, ⊥
	Phe36	14.0	C_δ	9.7(10.7)	$3.8(0.51)\times10^{-9}$	Proximal, //
	His33	16	C_8	13.1(14.0)	$4.2(0.69)\times10^{-12}$	Proximal, //
Pa cyt c_{551}	Tyr27	6.8	C_δ	3.5(5.2)	$9.1(0.30)\times10^{-4}$	Proximal, //
	Trp56	9.3	Cγ	4.7(6.2)	$8.3(0.41)\times10^{-5}$	Proximal, //
	Phe7	9.9	C_1	6.1(7.6)	$5.0(0.25)\times10^{-6}$	Proximal, ⊥
	Phe34	12.3	C_7	6.8(8.1)	$12.4(0.92)\times10^{-7}$	Proximal, //
	Trp77	12.4	C_1	7.0(9.2)	$8.3(0.10)\times10^{-7}$	Proximal, ⊥

† The distance, r_0, from the amino acid edge to the closest carbon atom on the porphyrin ring. The values in parenthesis are measured from the aromatic center to heme edge.
‡ The functional dependence assumed for the electronic overlap matrix element, with $\beta = 2\ \text{Å}^{-1}$, which is used to fit the photoreduction cross-sections, can be expressed as $V_0 e^{-\beta r_0} e^{-\beta\alpha q_0}$.

S6. Vibrational heating of heme.

It is possible that, during the excited state electron transfer, the excited vibrational temperature also plays a role. This could be one explanation why the photoreduction cross-section does not track the Soret absorption and is enhanced as the excitation is moved to the blue(20, 21). More importantly, the similarity in the short time kinetics between wt *Pa* cyt c_{551} and its F7A mutant (see Figs. S6.1 and Table S6), indicates that their electronic and vibrational decay pathways do not differ significantly. This is consistent with the idea that the difference in the ruffling distortion plays a primary role in determining the relative photo-reduction cross-sections, presumably by altering the inherent quantum yield, $\Phi = \tau_{eg}/\tau_r$, through reduced donor-acceptor electronic overlaps and Marcus parameters that affect τ_r, or possibly by changes in the heme non-radiative decay rate, τ_{eg}. The latter effect might arise if there was an increase in the porphyrin π^*-to-iron non-radiative decay rate due to more positive charge on the iron in the ruffled state.

Figure S6.1 The optical response as a function of excitation wavelength for the cyt c_{551} and its F7A mutant. The figure displays the ps kinetic response of wt *Pa* cyt c_{551} and its F7A mutant excited at different wavelengths ranging from 412 nm to 435 nm. The pump/probe pulse overlap produces a coherence coupling signal in the -200 fs to 200 fs region, which is removed in order to fit the kinetic response. From the fits, we determine that the vibrational relaxation time for wt *Pa* cyt c_{551} and the F7A mutant is similar and is in the range ~ 2-4 ps.

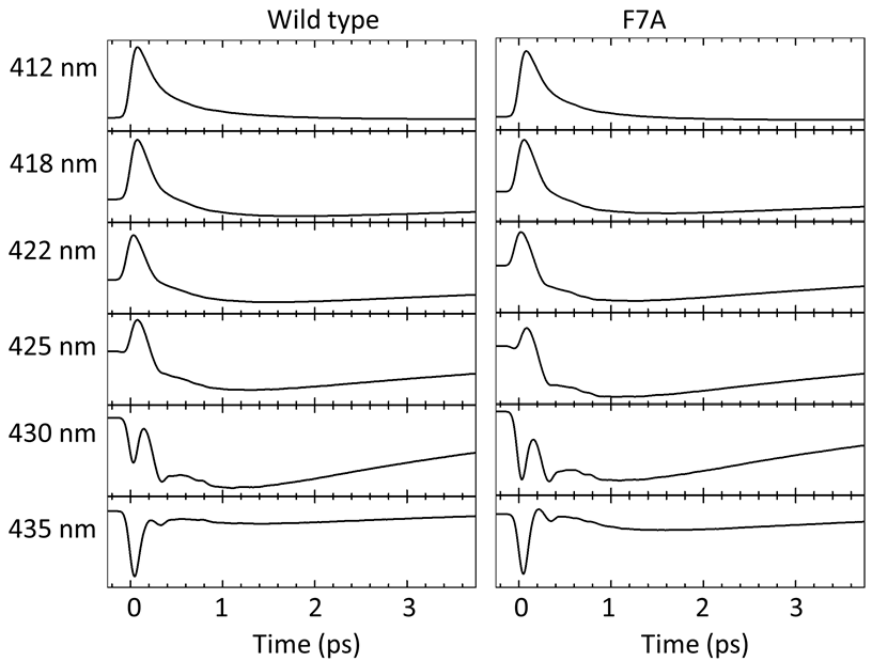

Table S6: Time constants for the population dynamics of ferric *Pa* cyt c_{551} wild type and F7A obtained by LPSVD. The kinetic rates are roughly independent of wavelength.

λ_{ex} (nm)	Decay time for wt (ps)	Amplitude for wt (a.u.)	Decay time for F7A (ps)	Amplitude for F7A (a.u.)
412*	0.15 (τ_1)	1.08	0.14 (τ_1)	1.26
	0.51 (τ_2)	0.58	0.53 (τ_2)	0.60
418	0.2 (τ_1)	0.49	0.16 (τ_1)	0.50
	0.60 (τ_2)	0.54	0.53(τ_2)	0.37
	4.6 (τ_3)	0.31	3.6 (τ_3)	0.36
422	0.12(τ_1)	0.36	0.31 (τ_1)	0.36
	0.52 (τ_2)	0.63	0.61(τ_2)	0.43
	4.6 (τ_3)	0.40	3.6 (τ_3)	0.61
425	0.22(τ_1)	0.43	0.12(τ_1)	0.42
	0.49 (τ_2)	0.52	0.52 (τ_2)	0.56
	3.6 (τ_3)	0.42	3.5 (τ_3)	0.59
430	0.61 (τ_2)	0.55	0.60(τ_2)	0.47
	2.8 (τ_3)	0.56	2.8(τ_3)	0.52
435**	2.0 (τ_3)	0.25	2.3 (τ_3)	0.21

* The ~ 4 ps (τ_3) kinetics at 412 nm are not extracted due to low amplitude.
**There is no observable τ_1 and τ_2 kinetics at 435 nm.

References

1. Russell BS, Zhong L, Bigotti MG, Cutruzzola F, & Bren KL (2003) Backbone dynamics and hydrogen exchange of Pseudomonas aeraginosa ferricytochrome C-551. *J. Biol. Inorg. Chem.* 8(1-2):156-166.
2. Borgia A, Bonivento D, Travaglini-Allocatelli C, Di Matteo A, & Brunori M (2006) Unveiling a hidden folding intermediate in c-type cytochromes by protein engineering. *The Journal of biological chemistry* 281(14):9331-9336.
3. Kubo M*, et al.* (2008) Low-frequency mode activity of heme: Femtosecond coherence spectroscopy of iron porphine halides and nitrophorin. *J. Am. Chem. Soc.* 130(30):9800-9811.
4. Gruia F, Ye X, Ionascu D, Kubo M, & Champion PM (2007) Low frequency spectral density of ferrous heme: perturbations induced by axial ligation and protein insertion. *Biophys. J.* 93(12):4404-4413.
5. Rosca F*, et al.* (2000) Investigations of coherent vibrational oscillations in myoglobin. *J. Phys. Chem. A* 104(18):4280-4290.
6. Kumar ATN, Rosca F, Widom A, & Champion PM (2001) Investigations of ultrafast nuclear response induced by resonant and nonresonant laser pulses. *J.Chem.Phys.* 114(15):6795-6815.
7. Gruia F*, et al.* (2008) Low-frequency dynamics of Caldariomyces fumago chloroperoxidase probed by femtosecond coherence spectroscopy. *Biochemistry* 47(18):5156-5167.

8. Gruia F, Ye X, Ionascu D, Kubo M, & Champion PM (2007) Low frequency spectral density of ferrous heme: perturbations induced by axial ligation and protein insertion. *Biophys.J.* 93(12):4404-4413.

9. Sun Y, Karunakaran V, & Champion PM (2013) Investigations of the low-frequency spectral density of cytochrome c upon equilibrium unfolding. *J. Phys. Chem. B* 117(33):9615-9625.

10. Roberts SA*, et al.* (2001) Ligand-induced heme ruffling and bent NO geometry in ultra-high-resolution structures of nitrophorin 4. *Biochemistry* 40(38):11327-11337.

11. Weichsel A, Andersen JF, Roberts SA, & Montfort WR (2000) Nitric oxide binding to nitrophorin 4 induces complete distal pocket burial. *Nature structural biology* 7(7):551-554.

12. Manthey JA, Boldt NJ, Bocian DF, & Chan SI (1986) Resonance Raman studies of lactoperoxidase. *The Journal of biological chemistry* 261(15):6734-6741.

13. Berezhna S, Wohlrab H, & Champion PM (2003) Resonance Raman investigations of cytochrome c conformational change upon interaction with the membranes of intact and Ca2+-exposed mitochondria. *Biochemistry* 42(20):6149-6158.

14. Ma JG, Vanderkooi JM, Zhang J, Jia SL, & Shelnutt JA (1999) Resonance Raman investigation of nickel microperoxidase-11. *Biochemistry* 38(9):2787-2795.

15. Frisch MJ et al. (2009) *Gaussian 09, Revision B.01; Gaussian, Inc.;Wallingford, CT*.

16. Schafer A, Horn H, & Ahlrichs R (1992) Fully Optimized Contracted Gaussian-Basis Sets for Atoms Li to Kr. *J. Chem. Phys.* 97(4):2571-2577.

17. Cave RJ, Siders P, & Marcus RA (1986) Mutual orientation effects on electron transfer between porphyrins. *J. Phys. Chem.* 90(7):1436-1444.

18. Wasielewski MR (1992) Photoinduced electron-transfer in supramolecular systems for artificial photosynthesis. *Chem. Rev.* 92(3):435-461.

19. Tusell JR (2011) Ph.D. Thesis (Montana State University).

20. Gu YG, Li PS, Sage JT, & Champion PM (1993) Photoreduction of heme-proteins - spectroscopic studies and cross-section measurements. *J. Am. Chem. Soc.* 115(12):4993-5004.

21. Lowenich D, Kleinermanns K, Karunakaran V, & Kovalenko SA (2008) Transient and stationary spectroscopy of cytochrome c: ultrafast internal conversion controls photoreduction. *Photochem Photobiol* 84(1):193-201.